JGR Oceans

RESEARCH ARTICLE
10.1029/2022JC019582

Scaling the Bubble Penetration Depth in the Ocean

A. Cifuentes-Lorenzen[1], C. J. Zappa[2], K. Randolph[1], and J. B. Edson[3]

[1]Department of Marine Sciences, University of Connecticut, Groton, CT, USA, [2]Ocean and Climate Physics, Lamont-Doherty Earth Observatory, Columbia University, New York, NY, USA, [3]Applied Ocean Physics & Engineering, Woods Hole Oceanographic Institution, Woods Hole, MA, USA

Key Points:

- The significant wave height and the effective wavelength were used to scale bubble penetration depths under open ocean conditions
- Both length scales successfully provide a penetration depth parameterization with the effective wavelength better collapsing the data

Correspondence to:

A. Cifuentes-Lorenzen,
alejandro.cifuentes@uconn.edu

Citation:

Cifuentes-Lorenzen, A., Zappa, C. J., Randolph, K., & Edson, J. B. (2023). Scaling the bubble penetration depth in the ocean. *Journal of Geophysical Research: Oceans*, *128*, e2022JC019582. https://doi.org/10.1029/2022JC019582

Received 13 JAN 2023
Accepted 17 AUG 2023

Author Contributions:

Conceptualization: A. Cifuentes-Lorenzen, C. J. Zappa, K. Randolph
Formal analysis: A. Cifuentes-Lorenzen, C. J. Zappa, K. Randolph
Funding acquisition: J. B. Edson
Investigation: K. Randolph
Methodology: A. Cifuentes-Lorenzen, C. J. Zappa, K. Randolph
Resources: C. J. Zappa
Validation: K. Randolph
Writing – original draft: A. Cifuentes-Lorenzen, C. J. Zappa, K. Randolph
Writing – review & editing: A. Cifuentes-Lorenzen, J. B. Edson

Abstract Bubble plume penetration depths have been identified as a key parameter linking subsurface turbulent kinetic energy (TKE) dissipation rates and whitecaps. From data collected in the Atlantic sector of the Southern Ocean, nominally 50°S 40°W, bubble plume penetration depths were estimated from Acoustic Doppler Current Profiler measurements of the acoustic backscatter anomaly. Bubble presence at depth was corroborated using independent measurements of optical scattering. Here, an effective wavelength, observations of significant wave height and atmospheric forcing were used to scale penetration depths of breaking waves under open ocean conditions. The parameterization was developed assuming a correlation between the observed penetration depth and an estimate of the TKE dissipation rate enhancement under breaking waves. The effective wavelength was defined from the effective phase speed based on a momentum and energy balance across the atmospheric wave boundary layer and was considered to be the largest actively wind-coupled wave and representative of large-scale breaking for wave ages ranging from 15 to 35 (i.e., $15 \leq \langle c_p/u_* \rangle \leq 35$). This yields a dimensional penetration depth parameterization in terms of inverse wave age and the length scales under consideration. The parameterization captures the bubble plume penetration depth with stronger forcing leading to deeper injections, reaching up to 9 m. Both length scales are effective at defining the depth of a wave-affected layer in terms of bubble presence with the effective wavelength better collapsing the data under mixed conditions with deeper plumes associated to larger fractional whitecap coverage.

Plain Language Summary The depth to which waves breaking at the ocean surface influence oceanic processes in the mixed layer, including the transfer of momentum, heat and gases between the atmosphere and ocean, is an ongoing and active area of research. Parameterizations and observations describing the vertical extent of wave-driven effects, including whitecaps and vertical jets associated with Langmuir circulation, are relevant for numerical circulation models and our understanding of wave breaking and dissipation dynamics. Here, observations of atmospheric and oceanic conditions, principally wind, wave, and inferred bubble plume penetration depths collected in the Atlantic sector of the Southern Ocean were used to build a parameterization for estimating the vertical extent of bubble injections and for inferring the depth of the wave-affected layer. These results suggest that wavelengths shorter than the dominant peak and significant wave heights properly weighted by atmospheric parameters are a good proxy for defining the extent of wave-driven bubble transport.

1. Introduction

Wave driven turbulence through wave breaking and Langmuir circulation (LC) has the capacity to modulate upper-ocean mixing, modifying the exchange of momentum, heat, and gases at the air-sea interface, and affect key biogeochemical cycles on Earth. Both mechanisms have been shown to impact the upper ocean turbulence structure under a different range of physical conditions (e.g., Kukulka & Brunner, 2015; Li et al., 2013). Ample evidence has suggested that wave breaking is responsible for an enhancement in subsurface turbulent kinetic energy (TKE) dissipation rates (e.g., Agrawal et al., 1992; Anis & Moum, 1995; Gemmrich et al., 1994; Sutherland & Kendall Melville, 2015; Terray et al., 1996; Zappa et al., 2016) by direct injection of TKE into the water column (e.g., Craig & Banner, 1994). Large-scale wave breaking leads to subsurface air entrainment, resulting in the formation of bubble plumes and surface foam (i.e., whitecaps) with profound consequences for air-sea interaction dynamics (e.g., Cavaleri et al., 2012; Gemmrich & Farmer, 2004; Woolf, 2005). As the surface manifestation of large-scale wave breaking, whitecaps have been identified as an ideal proxy for wave-modulated air-sea dependent processes (e.g., bib_anguelova_and_hwang_2016Anguelova & Hwang, 2016; Brumer et al., 2017a). Subsurface bubble plumes though are thought to have both direct and indirect impacts on the air-sea gas and

heat transfer (e.g., Asher & Wanninkhof, 1998; Farmer et al., 1993; Lamarre & Melville, 1991, 1996; Moore et al., 2011; Vagle et al., 2010; Zappa et al., 2007; Zavarsky et al., 2018). The small persistent bubbles injected by wave breaking can serve as excellent tracers of water motion (e.g., Wang et al., 2016) and used to define the extent of wave breaking (e.g., Thorpe, 1992). Under open ocean conditions, bubbles with penetration depths of up to 9 m were measured using optical methods (Randolph et al., 2013). Penetration depths ranging from 5 to 30 m have been reported for a wide range of conditions using acoustic methods (Derakhti et al., 2023; Strand et al., 2020; Vagle et al., 2010; Wang et al., 2016), providing insight into the potential extent of the wave-affected layer. Overall, wave breaking is a dissipative process where the volume of the two-phase flow injected by breaking is intimately connected to the subsurface TKE dissipation dynamics (e.g., Deane et al., 2016; Lamarre & Melville, 1991; Rapp & Melville, 1990). From this perspective, bubble plume penetration depths have been identified as a key parameter linking TKE dissipation rates and whitecapping, connecting wave-breaking characteristics to the subsurface TKE dissipation process (e.g., Anguelova & Hwang, 2016; Callaghan, 2018; Callaghan et al., 2016; Melville, 1996). Therefore, direct observations of penetration depths leading to robust parameterizations could aid in providing a link between a readily observable variable (whitecaps) and a difficult subsurface measurement (TKE dissipation rates) with very relevant implications to numerical models (e.g., Burchard, 2001).

Efforts have been largely focused on building a robust relationship between observed bubble plume characteristics and atmospheric and sea state conditions. Bubble penetration depths appeared to be proportional to the 10-m wind speed (U_{10}), with penetration depths increasing with wind magnitude (e.g., Derakhti et al., 2023; Strand et al., 2020; Vagle et al., 2010; Wang et al., 2016). Thorpe (1992) used the wavelength and significant wave height to scale the depth of the bubble injection, showing dependence on the inverse wave age and suggesting deeper penetration depths under strong forcing conditions. Penetration depths parameterized by Graham et al. (2004) showed a closer correlation between wind speed and penetration depths with some dependence on significant wave height.

Another relevant mechanism in the wave generation of turbulence is LC. Langmuir cells can also modify the subsurface TKE structure, enhance mixing and deepen the depth of the mixed layer, modulating atmosphere-ocean dynamics (e.g., Belcher et al., 2012; Gargett & Wells, 2007; Li & Fox-Kemper, 2017; McWilliams et al., 1997; Sullivan et al., 2007; Wu et al., 2019). Although LC does not directly generate bubbles, previous work by Plueddemann et al. (1996) showed mean bubble cloud depths associated with LC reaching up to 10 m below the sea surface.

Here, observations of bubble penetration depths in the open ocean were determined from measurements of acoustic backscatter and supported by independent optical observations at depth (Randolph et al., 2013). Penetration depths were used as a proxy to define the extent of the wave affected layer. Observations of penetration depths were considered a direct consequence of wave breaking with the potential modulation of LC, assessed in terms of the Langmuir number (e.g., Leibovich, 1983) and the threshold Langmuir number used by Belcher et al. (2012). These direct estimates of penetration depth were combined with local wave and atmospheric data in an effort to capture the relevant scale behind the observed penetration depths and propose a parameterization in terms of wind forcing and wave field dynamics and kinematics.

2. Methods

The depth of the wave-affected layer in the water column was defined using a combination of acoustic backscatter anomaly measurements and in situ optical measurements that indicated the presence of bubbles reaching maximum depths ranging between 6 and 9 m under open ocean conditions (Randolph et al., 2013). It is thought that within this layer, wave-driven turbulence directly injects bubbles through wave breaking and LC then transports bubbles to deeper depths in the water column (e.g., Li et al., 2013). Here, the acoustic backscattering anomaly was used to define the maximum depth of bubble plume injections. It is within this wave-affected layer specifically that scaling arguments for the observed penetration depths were explored.

2.1. Estimating Wind-Coupled Wave Scales

An energy and momentum balance across the wave boundary layer (WBL) on the atmospheric side were used to define an effective wave speed ratio of wind- to peak wave phase speeds (c_w/c_p) as described by Cifuentes-Lorenzen et al. (2018), where c_w represents the phase speed of the longest wind-coupled wave and provides the lower

frequency, that is, $f_w = g/(2\pi c_w)$, for coupled wind-waves. Peak wave characteristics were derived directly from the frequency spectra, such as peak phase speed (c_p), peak period (T_p) and frequency (f_p).

Parameterizations defined in terms of wind-wave scales (i.e., denoted by the subscript w) are expected to better capture the influence of wind coupled waves characterized by frequencies greater (i.e., higher frequencies) than the spectral peak frequency (f_p) relative to parameterizations relying on peak characteristics. The wind-waves characterized by these higher wave frequencies are expected to actively support momentum and energy transfer into the wave field and are assumed to capture breaking wave scales under open ocean conditions (e.g., Gemmrich & Farmer, 1999; Gemmrich et al., 2008). This is consistent with studies that have shown that the wavelengths of active breaking are only a fraction of the wavelength associate with the dominant spectral peak (e.g., Gemmrich & Farmer 1999; Gemmrich, 2005; Schwendeman et al., 2014). The set of observations and assumptions presented by Cifuentes-Lorenzen et al. (2018) led to a power-law parameterization of the form,

$$\frac{c_w}{c_p} = \mathrm{T}\left(\frac{u_*}{c_p}\right)^n \tag{1}$$

where c_w was defined as the effective phase speed, u_* is the atmospheric friction velocity and T and n were empirically determined coefficients estimated to be 1.42 and 0.59 respectively from momentum and energy considerations across the WBL during the 2008 Southern Ocean Gas Exchange Experiment (SO GasEx 08; Edson et al., 2011). The effective wavelength λ_w and wavenumber k_w can be determined directly from c_w using the deep-water dispersion relationship that is, $c_w = (g/k_w)^{1/2}$, $\lambda_w = 2\pi(k_w)^{-1}$.

2.2. Observations of Bubble Penetration Depths

The Acoustic Doppler Current Profiler (ADCP) deployed at approximately 1 m below the surface provided estimates of the high temporal resolution (0.4 Hz) acoustic backscattering anomaly used to track bubble injections. Before transforming the intensity (echo counts) to the power or acoustic energy (dB), the background signal from non-living and living particulate material, including a strong diurnal signal, was identified in the raw data (Figure 1) and removed to isolate the bubble plumes linked to wave breaking.

The ADCP intensity counts were transformed into acoustic power (dB) following Deines (1999) and Dave Ullman (*personal communication*). Conversion to acoustic power facilitates comparison with recent studies tracking bubbles using various instrumentation (e.g., Strand et al., 2020; Wang et al., 2016). An example of the backscattering signal is presented in Figure 2, including the raw signal of the backscatter anomaly from the ADCP for a 20 record (Figure 2a) and the signal after background removal (Figure 2b). The background signal in dB ($b(z)$) was defined as a function of depth for every 20-min segment based on the 95th percentile of the absolute value of the acoustic power at each depth. The intensity and extent of the background signal was initially determined experimentally through observations of the signal amplitude. The average background amplitude was related to biota and ambient noise ranged between −60 and −70 dB, consistent with previous observations (e.g., Dahl & Jessup, 1995) and exhibited a depth dependence. The background removed signal ($B_{\mathrm{corr}}(z)$) was determined for each profile (in the 20-min segment) as $B_{\mathrm{corr}}(t,z) = |B(t,z)| - |b(z)|$, where $B(z)$ is the observed acoustic power array (i.e., $n \times m$, based on sampling and averaging considerations) and $b(z)$ is a vector ($n \times 1$). The final corrected acoustic power array was then averaged over the 20 min and adjusted to obtain the original magnitude of the signal to retrieve penetration depths based on an acoustic threshold.

This process removes the background signal linked to biota and isolates potential breaking at the surface (Figure 2).

The averaging window was selected to best match the time stamp of concurrent wave and meteorological set of observations during the SO Gasex08 field campaign. Finally, observed penetration depths are reported from a wave-following frame of reference and therefor relative to the immediate surface.

Penetration depths were then defined relative to the surface for a backscattering signal with a minimum of −55 dB (Figure 3). This threshold was consistent with previously reported values used to identify bubbles (e.g., Dahl & Jessup, 1995; Thorpe, 1986; Trevorrow et al., 2003; Wang et al., 2016).

Bubbles (radii less than 60 μm) at comparable depths were detected in measurements of near forward scattering and critical angle scattering for bubbles (~80°) supported the presence of bubbles (Randolph et al., 2013). Figure 3 shows 20 min averages of the background removed backscattering signal for the two periods of interest.

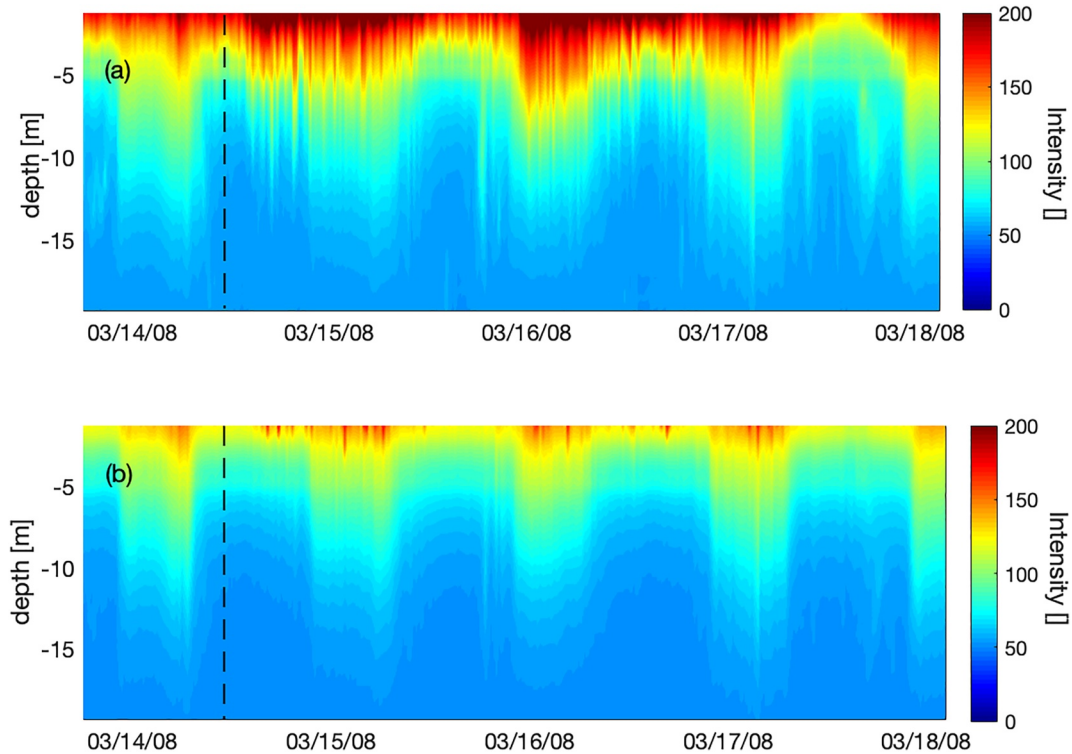

Figure 1. Example of the raw signal from Acoustic Doppler Current Profiler used in this study (a) raw signal versus depth versus time (b) Background signal isolating the diurnal cycle and the vertical phytoplankton migration in the water column. Black dashed line denotes the approximate time related to the example provided in Figure 2.

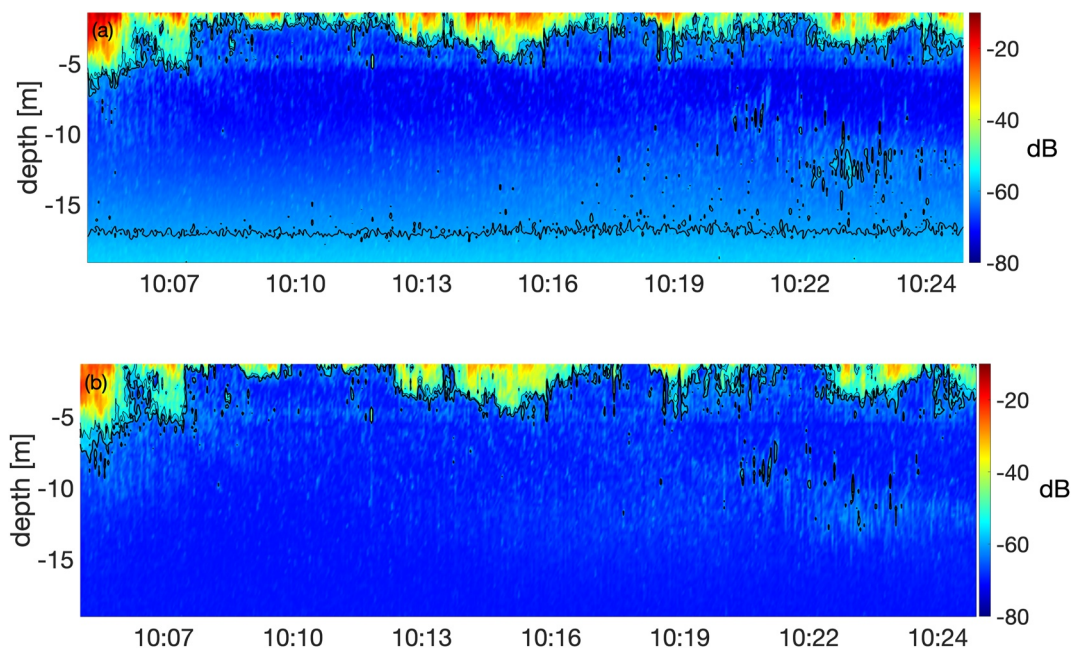

Figure 2. Example of the backscattering anomaly for a 20-min segment during 14 March 2008 with a mean wind speed of 7.4 m s^{-1} and a mean significant wave height of 2.64 m. (a) Top panel shows the raw amplitude of the raw signal (dB). Black contours delineate the −60 and −50 dB range (b) Bottom panel shows the raw signal after the background backscattering is removed. The removal of the background isolates the surface structure of enhanced acoustic backscatter associated to wave breaking and the presence of bubbles also removing backscattering associated to biological processes.

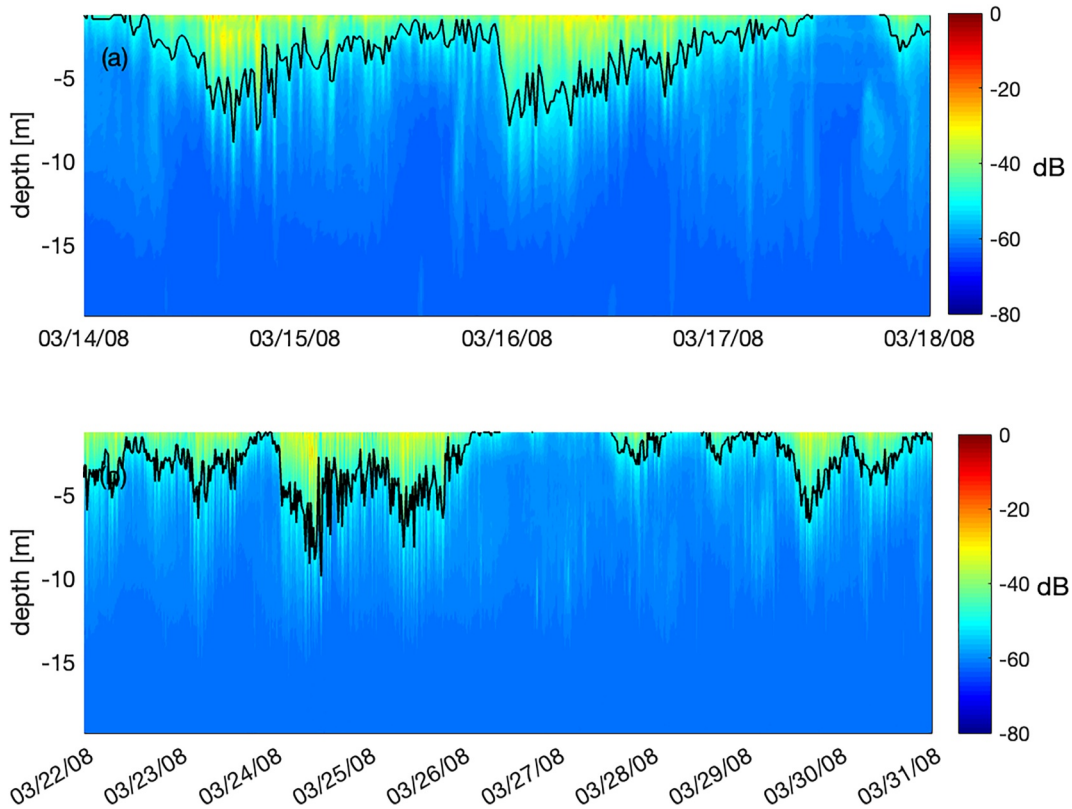

Figure 3. Full background removed backscattering signal for both periods under consideration. Top panel (a) Period 1 background removed signal (14–18 March). Bottom panel (b) Period 2 background removed signal (22–31 March, Period 2). The black line represents the penetration depth linked to wave breaking and bubble injections into the water column. The apparent resolution difference is due to the second period of interest being longer (time) than period 1.

The penetration depth linked to these observations is shown in black (solid black line). During both periods there are times with persistent bubble presence close to the surface with more sporadic events penetrating deeper in the water column (e.g., Thorpe, 1992). Penetration depth estimates were complemented with meteorological data, including estimates of atmospheric momentum and energy flux and with wave field spectra and wave statistics.

3. Field Campaign and Observations

The Southern Ocean Gas Exchange Experiment was designed to investigate the processes governing gas exchange at high winds by implementing the dual tracer technique (Ho et al., 2011) and the direct covariance (eddy-correlation) method (Edson et al., 2011). The experiment took place in the Atlantic sector of the Southern Ocean (nominally 50°S 40°W; Figure 4) on the National Oceanographic and Atmospheric Adminsitration (NOAA) Ship *RV Ronald H. Brown* from March through April 2008.

Atmospheric measurements were based on a meteorological package mounted on the jack-staff of the ship consisting of three Gill R3 sonic anemometers for fast response velocity and temperature measurements; two Vaisala PTU200 sensors to measure pressure; temperature and humidity; and three open path Licor 7500 to measure atmospheric water vapor and CO_2 concentrations. On the ocean side a drifting autonomous buoy was designed by NOAA and the Pacific Marine Environmental Laboratory (PMEL) and deployed at the site (Figure 4) to make high frequency physical and biogeochemical measurements (i.e., MAPCO$_2$ buoy) in the tracer patch during the experiment (Moore et al., 2011). The buoy was ∼1.5 m in diameter and had an approximate vertical profile of 2 m. Below the buoy was a 118 m string of instruments and 6 tubular canvas drogues that were 10 m long by 1 m in diameter. At the bottom of the string was 350 pounds of weight. Central to this study, the MAPCO$_2$ buoy was equipped with a Teledyne RD instruments 1,200 KHz ADCP that measured vertical profiles of 3-axis velocity over 20 m of water column with a blanking distance of 0.44 m and the first bin at 0.8 m from the instrument head.

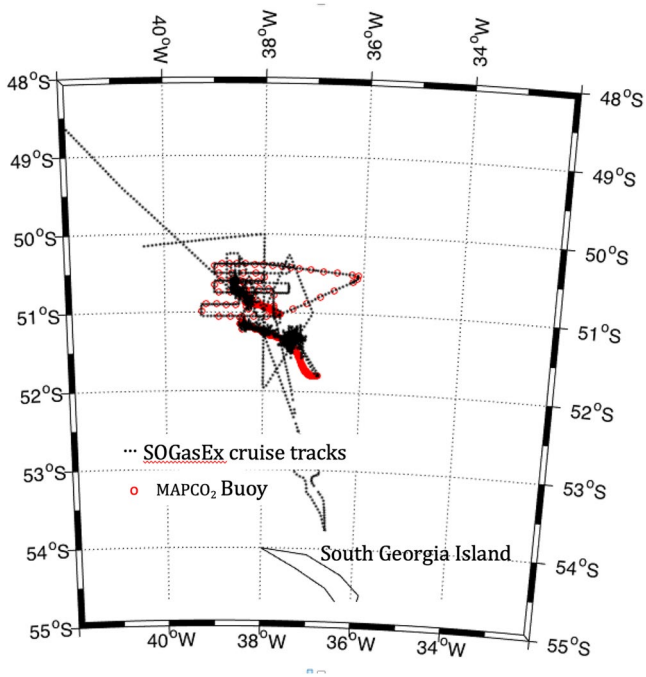

Figure 4. R/V Brown cruise tracks and the overlapping $MAPCO_2$ drifter tracks during the Southern Ocean Gas Exchange Experiment 2008.

There were 74 bins with a cell size of 25 cm. A profile was sampled every 2.5 s throughout the deployments. ADCP measurements are reported relative to the surface at approximately 1.5 m. The buoy was deployed on 08 March 2008 and recovered on 31 March 2008. The GPS location of the buoy was transmitted via Iridium satellite to NOAA/PMEL once per hour. These data were automatically processed and posted to a web site that could be accessed from the NOAA Ship Ron Brown to get near real time information about the location of the MAPCO2 buoy.

The sonic anemometers were paired with inertial measurement units (IMU; Systron-Donner MotionPaks) to remove platform motion before calculation of the fluxes (Edson et al., 1998). The experiment was carried out under moderate to high winds ($5 \leq U_{10} \leq 18$ m s^{-1}) with a severe wind event ($U_{10} > 18$ m s^{-1}) encountered at the end of the field campaign (Figure 5). Wave statistics were retrieved from an X-Band radar (i.e., the WaMoS system developed by OceanWaveS), a laser altimeter (i.e., RIEGL) and a microwave sensor (i.e., the Tsurumi-Seiki microwave Doppler radar TSK). The instrumentation resolved a spectral frequency in the 0.035–1.2 Hz range with a frequency slope of f^{-4} after merging the WaMoS (low frequency) with the RIEGL (high frequency) with a good signal to noise ratio (Cifuentes-Lorenzen et al., 2013). The data used in the present study was selected from periods in which the speed over ground (SOG m s^{-1}) was less or equal than 3 m s^{-1} to minimize doppler effects in measurements of the wave spectra and facilitate correction (Cifuentes-Lorenzen et al., 2013).

The wave age, defined as the ratio of peak phase speed to atmospheric friction velocity, c_p/u_*, was used to characterize the sea state as young (developing), mature (developed) or old (decaying). During the field campaign we observed on average mature or fully developed seas with an average wave age of $\langle c_p/u_* \rangle = 65$ (brackets denote temporal averaging). Significant wave heights (H_s) averaged 3.2 m throughout the experiment, exceeding 10 m under severe conditions (Figure 5). The scale of the dominant waves (spectral peak) show a frequency range between $0.08 < f < 0.12$ Hz, which we associate with the background swell component of the wave field. The relative directional homogeneity of the wind forcing leads to the wind-wave peak to develop in the same direction (±40°) as exhibited by the swell component, with the wind-waves riding on top of the swell component. Under these conditions, detection of the wind-driven wave component was difficult as the longer more energetic waves at the spectral peak shadowed the shorter wind-driven spectral range.

4. Results

Two continuous periods during the SO Gasex deployment provided the backscatter anomaly used to directly define bubble penetration depths (p_d). High temporal resolution of backscattering anomalies were linked to wave breaking bubble injections reaching down to 6–9 m at times. The periods under consideration were selected as they presented ideal conditions under open ocean with relatively strong forcing leading to a range of developed to young seas (i.e., $15 \leq \langle c_p/u_* \rangle \leq 35$). From a LC perspective, the Langmuir number (L_a) had mean values of 0.30 and 0.35 respectively placing the regime at the limit between wind and wave driven turbulence minimizing a wave-driven regime with active LC (Belcher et al., 2012) which was not fully resolved with these observations.

4.1. Penetration Depths

During the first period (14–18 March, Period 1) the significant wave height had a mean value of $\langle H_s \rangle$ 3.21 ± 0.39 m with a mean wind speed $\langle U_{10} \rangle$ of 13.42 m s^{-1} reaching a maximum value of 16.20 m s^{-1}. The mean penetration depth ($\langle p_d \rangle$) from the backscatter anomaly was: $\langle p_d \rangle = -3.2 \pm 1.8$ m with maximum penetration depths reaching −8.9 m. The second period, 21–31 March (Period 2), exhibited larger significant wave heights with $\langle H_s \rangle = 4.75 \pm 1.19$ m and similar wind speeds $\langle U_{10} \rangle = 13.34$ ms^{-1}, reaching a maximum value of 16.08 m s^{-1}. The backscatter anomaly estimated a mean penetration depth $\langle p_d \rangle = -2.5 \pm 1.9$ m with maximum penetration

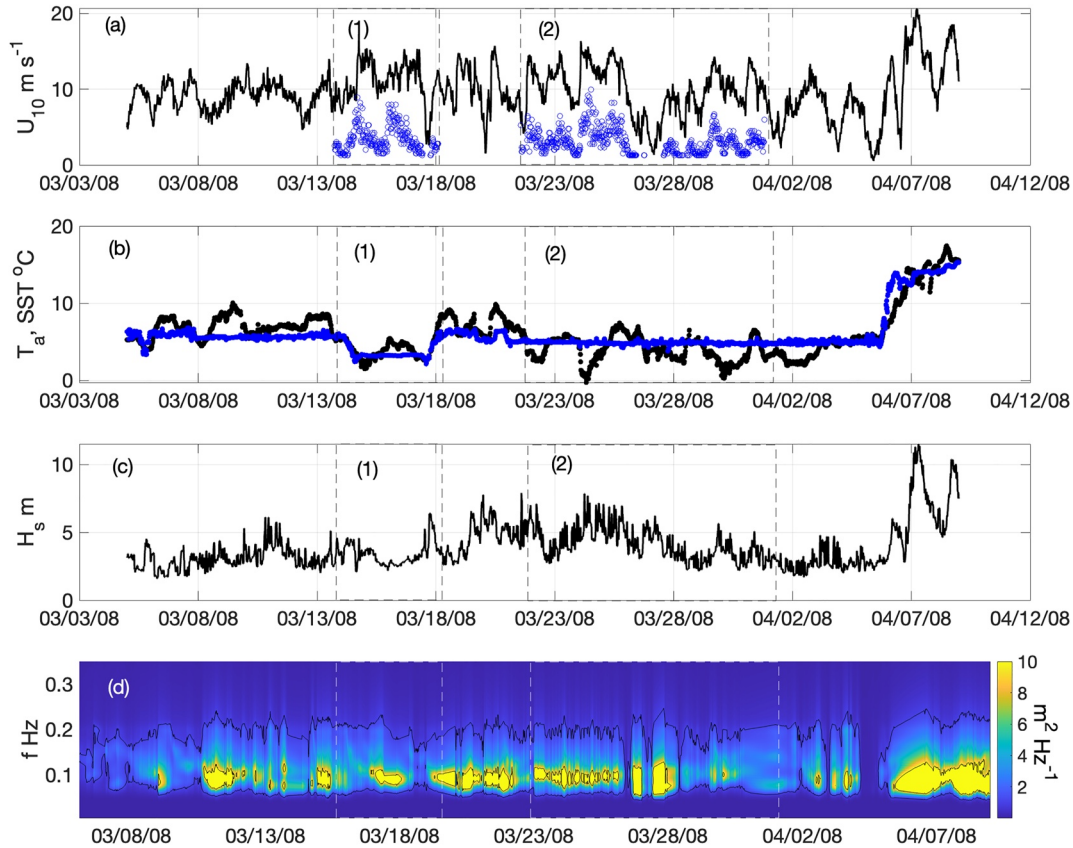

Figure 5. Overall conditions. 5a: Wind speed black line. Observed penetration depths (absolute value) blue circles. 5b: Air Temperature (10 m) black line, Sea Surface Temperature blue line. 5c: Significant wave height. 5d: Frequency spectra, time. Dashed black rectangles show both periods of interest (period 1 and period 2 labeled accordingly).

depths reaching −9.0 m. Penetration depths for both periods are plotted in Figure 6 as a function of significant wave height and the effective wavelength, $^{2\pi}/_{k_w}$. The significant wave height provides a length scale physically related to the mean of the highest third of the waves and an estimate of the wave amplitude.

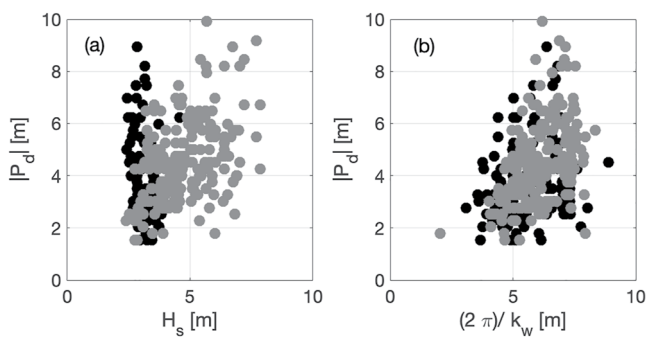

Figure 6. Absolute values of observed penetration depth (p_d) versus significant wave heights (a) and effective wavelength (b). Data selected to satisfy a wave age range of $15 \leq \langle c_p/u_* \rangle \leq 35$. Period 1 (black) and Period 2 (gray). Period 1 mean wind speed $U_{10} = 13.4$ m s^{-1} ± 1.13, mean significant wave height $\langle H_s \rangle = 3.21$ m ± 0.39, a mean observed penetration depth $\langle p_d \rangle = -3.2 \pm 1.8$ m and mean peak phase speed 14.8 m s^{-1}. Period 2 has a mean wind speed U_{10} 13.34 m s^{-1} +/− 1.11, mean significant wave height 4.74 ± 1.21 m, mean observed penetration depth $\langle p_d \rangle = 4.5 \pm 1.5$ and mean peak phase speed 16.1 m s^{-1}.

The proposed parameterization for actively wind coupled waves represents the scale of the wind-driven waves and, under the equilibrium assumption, all wind energy inputted into the wave field is dissipated through wave breaking and the wind-coupled wave scales (λ_w) represent the upper cut-off for breaking under open ocean conditions. The effective wave scales were derived from Equation 1 under forcing conditions in the range: $15 \leq \langle c_p/u_* \rangle \leq 35$.

The combination of both periods of interest provides 320 20-min averaged data points for comparison and analysis. The agreement between observations and both depth-scaling arguments was assessed based on the index of agreement, d (Equation 2), a measure of the model skill (parameterization here), and is defined by Willmott et al. (1985) as

$$d = 1 - \left[\sum_{i=1}^{N} \frac{(X_i - x_i)^2}{\sum_{i=1}^{N} (|X_i - \langle x \rangle| + |x_i - \langle x \rangle|)^2} \right], \quad (2)$$

where the brackets denote temporal averages. The index of agreement ranges between zero (no agreement) and 1 (perfect agreement).

Table 1
Index of Agreement (Equation 2) Between Depth Scaling Arguments (i.e., $2\pi/k_w$ and H_s) and the Observed Penetration Depth From the Backscatter Anomaly (p_d)

d	Period 1 (14–18 March) (n = 112)	Period 2 (21–31 March) (n = 208)
$2\pi/k_w$ versus $\lvert p_d \rvert$	0.48	0.55
H_s versus $\lvert p_d \rvert$	0.31	0.65

Period 1 shows a 0.48 index of agreement between the effective wavelength and the observed penetration depth with a root-mean-square error (RMSE) of 2.4 m. Using the significant wave height yields a 0.31 index of agreement and a RMSE of 1.8 m. During Period 2, the effective wavenumber as a penetration depth scaling argument has an index of agreement of 0.55 and an RMSE of 2.1 m. The significant wave height as a scaling argument has an index of agreement of 0.65 and an RMSE of 1.5 m.

Thorpe (1992) analyzed the scaling of the average bubble plume penetration depth relative to the wavelength of the dominant waves (i.e., p_d/λ_p) and significant wave height. These values were explored in the context of the inverse wave age for $0.6 < {}^{U_{10}}/_{c_p} < 2$ where p_d/λ_p ranged from 0.04 to 0.2. This approach was based on the dominant waves (i.e., spectral peak) of the wave field, which makes sense under younger developing seas or purely wind-driven seas. For older seas (${}^{U_{10}}/_{c_p} < 0.82$), breaking in the spectral peak is expected to be minimized and displaced toward higher frequencies, within shorter, steeper waves (Ding & Farmer, 1994; Gemmrich et al., 2008; Kitaigorodskii, 1998). Therefore, open ocean conditions require a different spectral region to capture the appropriate breaking scales and link bubble penetration depths to breaking waves (Table 1).

Following Thorpe (1992) the ratio of effective wavelength to observed penetration depth (${}^{2\pi k_w}/_{p_d}$) was compared against the average wave age (Table 2). The ratio was also defined using wave heights (${}^{H_s}/_{p_d}$) (Table 2).

4.2. Penetration Depths and Atmospheric Forcing

Under a steady state (i.e., wind-wave equilibrium conditions) the wave field is expected to exhibit a balance between wind energy input, non-linear transfer and dissipative processes including wave breaking. Although dissipative processes go beyond purely large-scale breaking (e.g., micro-breaking), the assumption presented here is that wind energy input is approximately balanced to the overall dissipative processes with large-scale breaking being the dominant term (e.g., Callaghan, 2018) and non-linear interactions mainly redistributing energy (Anguelova & Hwang, 2016). From this perspective, input and dissipation rates can be used to constrain breaking dynamics. The wind-driven energy input (E_{in}) to the wave field (e.g., Gemmrich & Farmer, 1999; Gemmrich et al., 1994; Terray et al., 1996) can be estimated in terms of an effective phase speed (c_w). Neglecting the viscous component, the input can be written as:

$$E_{\text{in}} = \tau_t \, c_w \tag{3}$$

where E_{in} is the wind energy going into the wave field, τ_t corresponds to the total momentum flux above the interface, that is, $\tau_t = \rho_a u_*^2$. Equation 3 captures the energy input from wind to waves where the phase speed (c_w) is generally a fraction of the peak phase speed under open ocean conditions.

In the absence of waves the ocean surface could be defined as a rigid wall, then TKE dissipation rates would follow from:

$$\varepsilon_p(z) = \frac{(u_*^w)^3}{\kappa \, z}, \tag{4}$$

where κ is the von Karman constant and z is the distance from the wall that is, boundary or the air-sea interface here. In this scenario (in the absence of buoyancy production/consumption of TKE), dissipation would be balanced by shear production. The water-side friction velocity in Equation 4 (u_*^w) follows from a momentum balance between atmosphere and the ocean, $\rho_a u_*^2 = \rho_w (u_*^w)^2$, where the left hand side represents the total atmospheric momentum flux in terms of the friction velocity (u_*). The depth integrated TKE dissipation rate was initially defined between the absolute value of the observed penetration depth ($\lvert p_d \rvert$) derived directly from backscattering anomalies and z', where z' is a reference depth close to the surface (here selected to $z' = 1$ based on the deployment configuration i.e., from a wave-following frame of reference looking down).

Table 2
Mean Wave Age ($\langle c_p/u_* \rangle$), Mean Significant Wave Height ($\langle H_s \rangle$) and Mean Ratio of Effective-Wave-Scale to Observed Penetration Depth ($\langle {}^{2\pi k_w}/_{p_d} \rangle$) for Both Periods of Interest

	Period 1 (14–18 March)	Period 2 (21–31 March)
$\langle c_p/u_* \rangle$	27.81 ± 4.25	30.43 ± 2.80
$\langle H_s/\lvert p_d \rvert \rangle$	0.97 ± 0.40	1.14 ± 0.39
$\langle {}^{2\pi/k_w}/_{\lvert p_d \rvert} \rangle$	1.66 ± 0.67	1.46 ± 0.47

Note. The data was selected to satisfy a wave age range of $15 \leq \langle c_p/u_* \rangle \leq 35$.

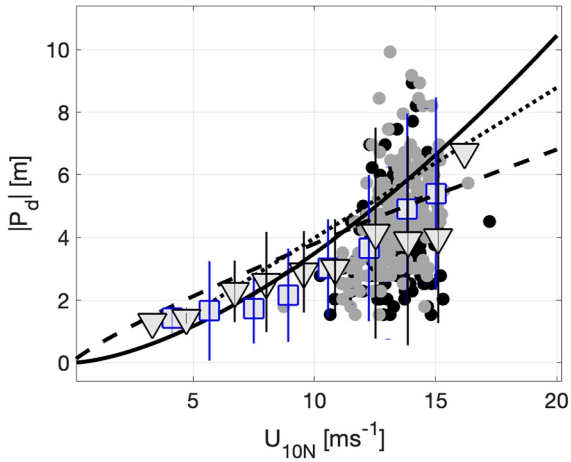

Figure 7. Observed penetration depths as a function of neutrally adjusted wind speed (U_{10N}). Data used in the analysis is plotted in black and gray dots (period 1 and 2 respectively) only for wind speeds between 10 and 15 m s^{-1}. Black triangles show all the wind bin averaged data ± two standard deviation (period 1). Blue squares show all the bin averaged data (period 2) ± two standard deviations. Black solid line is a parameterization proposed by Derakhti et al. (2023): $\overline{D}_{bp} = 0.092(U_{10N})^{1.58}$. Black dashed line is a parameterization proposed by Derakhti et al. (2023) based on a different thresholding method for detection of bubbles: $\overline{D}_{bp} = 0.55(U_{10N})^{0.84}$. Black dotted line is the parameterization presented by Vagle et al. (2010), $\delta = -0.83 + 0.481{*}U_{10}$, in this case evaluated using the neutral wind speed.

$$\varepsilon_D = \rho_w \frac{(u_*^w)^3}{\kappa} \int_{z'}^{|p_d|} z^{-1} dz \tag{5}$$

It then follows,

$$\varepsilon_D = \rho_w \frac{(u_*^w)^3}{\kappa} \ln\left(|p_d|/z'\right) \tag{6}$$

Equation 6 represents the TKE dissipation rate in the absence of waves integrated through the wave-affected layer and provides a wave-free shear-production driven estimate of the TKE in the wave affected layer. Assuming a balance between the wind energy input and the wave-breaking dissipation rates (e.g., Thomson et al., 2016), then a means to quantify wave-breaking enhancement of TKE relative to a rigid-wall-scaling can defined through the ratio of the wind energy input to the depth integrated TKE dissipation given by:

$$\Gamma = E_{\text{in}}/\varepsilon_D, \tag{7}$$

with the expectation that through the wave-affected layer (in terms of the TKE dissipation rate enhancement) $\Gamma \gg 1$ with the wave breaking driven enhancement constraint to this layer (e.g., Drennan et al., 1992, 1996). Previous work suggests that stronger forcing leads to deeper penetration depths (e.g., Derakhti et al., 2023; Graham et al., 2004; Strand et al., 2020). However, evaluating the behavior of observed penetration depths as a function of wind speed and wind energy input alone exhibits a low index of agreement. For example, observations show $d = 0.43$ and $d = 0.41$ for period 1 and 2 respectively for $|p_d|$ versus E_{in}. This is also the case for wind speed. Figure 7 presents the relation between wind speed and the observed penetration depths and three wind speed only dependent parameterizations presented as a reference.

Bin averaged observations for a wider range of wind speeds are consistent with previous parameterizations (Figure 7). Nonetheless, the wind speed alone has a low index of agreement and fails to capture the variance under stronger forcing (Table 3). The large variance observed in the penetration depths could be a consequence of a wave state dependence not fully captured by the wind forcing nor the energy input term and be related to a wave-driven transport (Figure 7). Nonetheless, the observed penetration depths are directly proportional to the estimate of the dissipation rate in the wave-affected layer through Equation 6 with correlation coefficients of 0.72 and 0.79 for period 1 and 2 respectively. This is in part a consequence of a self-correlation by means of p_d versus $\ln(p_d)$ when evaluating $|p_d|$ versus ε_D. Despite the self-correlation, Equation 6 maintains the atmospheric forcing dependence through $(u_*^w)^3$ as the water friction velocity follows from an air-sea momentum balance at the interface.

Taking advantage of the better correlation of penetration depths with ε_D the proposed dimensionless scaling follows from the inverse of Equation 7 assuming a direct relationship between bubble penetration depth and the depth of the TKE enhancement,

$$|p_d|/L = \Gamma^{-1} \tag{8}$$

where L represents the length scale under consideration. Here, for the significant wave height (i.e., H_s), $|p_d|/H_s = \Gamma^{-1}$ and in terms of the effective wavelength $|p_d|/2\pi(k_w)^{-1} = \Gamma^{-1}$. The right hand side of Equation 8 will retain the observed penetration depth (i.e., $|p_d|$) in the logarithmic function as a consequence of the integration limits defined in Equation 5. The substitution of E_{in} for $\rho_a u_*^2 c_w$ and ε_D for $\rho_w \frac{(u_*^w)^3}{\kappa} \ln(|p_d|/z')$ leads to $|p_d|/L$ being proportional to the inverse wave age that is, $\propto u_*/c_w$ (i.e., wind forcing) where c_w is the

Table 3
Absolute Value of the Observed Penetration Depths $|p_d|$ for Both Periods of Interest as a Function of Wind Speed (U_{10N}) and Wind Energy-Input (E_{in})

d	Period 1 (14–18 March) (n = 112)	Period 2 (21–31 March) (n = 208)
$\|\boldsymbol{p_d}\|$ versus $\boldsymbol{U_{10N}}$	0.33	0.36
$\|\boldsymbol{p_d}\|$ versus $\boldsymbol{E_{\text{in}}}$	0.37	0.41

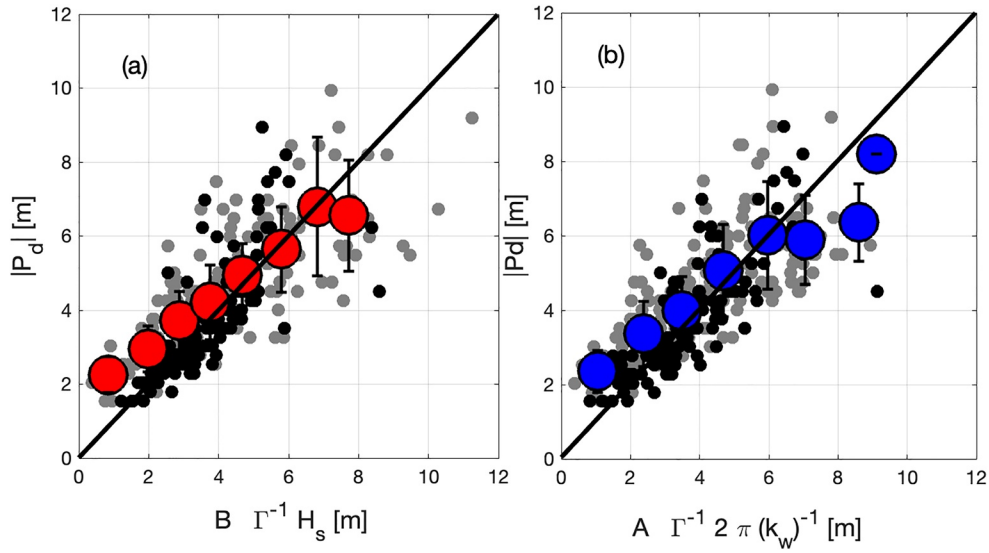

Figure 8. The proposed scaling arguments: $A\,\Gamma^{-1}(2\pi/k_w)$ and $B\Gamma^{-1}(H_s)$ versus the observed penetration depth (absolute value). The red circles on (a) and blue circles on (b) represent bin averages plus/minus one standard deviation for both periods combined. The coefficient B was determined to be: 71.6 and 38.2 for period 1 and 2 respectively. The coefficient A was determined to be 38.4. and 29.7 for period 1 and 2 respectively. Correlation coefficient (R^2) for Period 1 is 0.87 based on the significant wave height and 0.66 based on the effective wavelength. For period 2 R^2 is 0.79 for significant wave height and 0.83 for the effective wavelength.

effective phase speed. Solely on dimensional grounds this implies, $|p_d| = f(u_*/c_w, H_s, \lambda_w)$ consistent with recent work by Derakhti et al. (2023).

A dimensional 1:1 relationship between $\Gamma^{-1}H_s$ and $\Gamma^{-1}2\pi(k_w)^{-1}$ and the observed penetration depth follows simply by introducing a constant coefficient. The proposed scaling arguments are finally stated as: $A\,\Gamma^{-1}(2\pi/k_w)$ and $B\Gamma^{-1}(H_s)$ and yield a dimensional length of penetration depths associated to the wave state under open ocean conditions. Table 4 shows the index of agreement for both periods of interest and introduces two numerical constants experimentally determined: A and B. The A constant has values of 38.4 and 29.7 and B has values of 71.6 and 38.2 for the first and second period of interest respectively.

Figure 8 shows the comparison of this approach to the observations and length scales with the index of agreement presented in Table 4. Both length scales weighted by the ratio Γ^{-1} capture the variance in the observed penetration depths and better collapse the data. The largest deviations from the 1:1 line are observed for penetration depths larger than 6–7 m. It is possible that the observed penetration depths larger than 6–7 m are decoupled from the proposed breaking length scales and atmospheric forcing suggesting another mean for transport not resolved in the current parameterization.

At this point the improvement in the correlation is tied in part to a self-correlation by means of p_d versus $\ln(p_d)$ and follows as a direct consequence of assuming that the bubble transport (i.e., observed penetration depth) can be directly linked to the depth of the expected TKE dissipation rate enhancement (relative to the wall scaling) defined by the integration limits in Equation 6.

Table 4
Wave Breaking Weighted Penetration Depth Scales

d	Period 1 (14–18 March) (n = 112)	Period 2 (21–31 March)(n = 208)
$\boldsymbol{A\,\Gamma^{-1}(2\pi/k_w)}$ versus $\boldsymbol{|p_d|}$	0.98	0.83
$\boldsymbol{B\Gamma^{-1}(H_s)}$ versus $\boldsymbol{|p_d|}$	0.95	0.85

Note. The absolute value of the observed penetration were used in the evaluation of Equation 2 The coefficients A and B where determined independently for each segment under consideration.

A change in the integration limits between z' and L leads to,

$$|p_d|/L = \Gamma^{-1} = \alpha^{1/2}\,\kappa^{-1}\left(\frac{u_*}{c_w}\right)\ln(L/z') \tag{9}$$

where α is the density ratio (ρ_a/ρ_w). Equation 9 avoids any self-correlation and assumes that the wave-affected layer can be constraint by the length scale L linking bubble injection and TKE dissipation rate enhancement. Equation 9 follows from defining H_s and $2\pi(k_w)^{-1}$ as integration limits in Equation 6. A

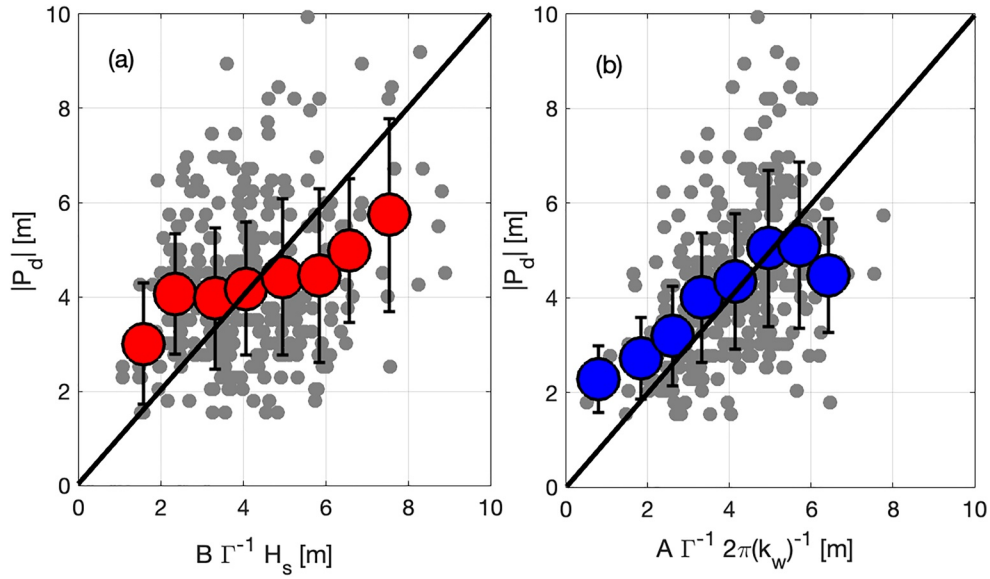

Figure 9. The proposed scaling arguments: $A\,\Gamma^{-1}(2\pi/k_w)$ and $B\Gamma^{-1}(H_s)$ versus the observed penetration depth (absolute value). Equation 7 now leads to: $\rho_w \frac{(u_*^w)^3}{\kappa} \ln(L/z')$ and defines Γ^{-1} without the use of observed penetration depths solely relying on independent estimates of the wave-affected layer. Gray dots are all the observations for both periods under consideration. The colored circles in (a) and (b) are bin-averaged estimates plus/minus one standard deviation for both periods in consideration.

comparison including the numerical coefficients A and B previously defined to achieve a 1:1 and plotting observed penetration depths as a function of $A\,\Gamma^{-1}(2\pi/k_w)$ and $B\Gamma^{-1}(H_s)$ with no implicit self-correlation (Equation 9) is presented in Figure 9.

The RMSE is presented in Table 5 and the index of agreement for the scales and periods are presented in Table 6. The largest deviations from the 1:1 line were observed for penetration depths larger than 5 m for $A\,\Gamma^{-1}(2\pi/k_w)$ (Figure 9b). The dimensional parameterization based on significant wave heights appears to be well behaved for a narrower range of observations with an a RMSE of 1.3 m up to 5 m. Figure 9b suggests that the effective wavelength better captures the penetration depth scaling up to 5 m with a RMSE of 0.81 m, potentially better linking wave breaking and penetration depth scales by better identifying the wind-driven range of the wave field. In this case the transport of bubbles through atmospheric forcing would be limited to depth proportional to the scale of the wind driven wave. This is consistent with previous studies that have noted the relevance of wave statistics to better capture air-sea interaction dynamics and produce relevant parameterizations (e.g., Brumer et al., 2017b).

4.3. Penetration Depths and Whitecap Coverage

An ongoing area of investigation focuses on elucidating the link between the surface manifestation of breaking and subsurface physics (e.g., Anguelova & Hwang, 2016; Callaghan, 2018; Cifuentes-Lorenzen & Randolph, 2020; Schwendeman & Thomson, 2015; Sutherland & Melville, 2015) with key parameters such as breaking period (e.g., Anguelova & Hwang, 2016) and bubble plume penetration depths (e.g., Callaghan, 2018). Based on observations from SO Gasex 08, Figure 10 shows the behavior of observations of whitecap fractional coverage (Brumer et al., 2017a; Randolph et al., 2017) as a function of observed penetration depths during both periods of interest.

Brumer et al. (2017a) presented whitecap coverage parameterizations derived from digital imaging for the SO Gasex 2008 campaign and concluded on the relevance of wave field statistics to improve whitecap parameterizations. Also, Randolph et al. (2017) derived an estimate for fractional whitecap coverage based on spectral radiometry in an effort to identify different

Table 5
Root-Mean-Square Error for the Proposed Wave Breaking Weighted Penetration Depth Scales

RMSE (m)	Period 1 (14–18 March) (n = 112)	Period 2 (21–31 March) (n = 208)
$\boldsymbol{A\,\Gamma^{-1}(2\pi/k_w)}$ versus $\boldsymbol{\lvert p_d \rvert}$	0.50	1.07
$\boldsymbol{B\Gamma^{-1}(H_s)}$ versus $\boldsymbol{\lvert p_d \rvert}$	0.74	1.25

Note. The coefficients A and B were determined independently for each selected period of time.

Table 6
Wave Breaking Weighted Penetration Depth Scales

d (Equation 8)	Period 1 (14–18 March) (n = 112)	Period 2 (21–31 March) (n = 208)
$\boldsymbol{A}\,\Gamma^{-1}(2\pi/k_w)$ versus $\lvert p_d\rvert$	0.74	0.87
$\boldsymbol{B}\Gamma^{-1}(H_s)$ versus $\lvert p_d\rvert$	0.39	0.76

Note. Equation 8 was modified to eliminate the self-correlation implicit in the proposed scaling argument. The coefficients A and B where determined independently for each segment under consideration. The index of agreement is presented for both periods for a 0–6 m range.

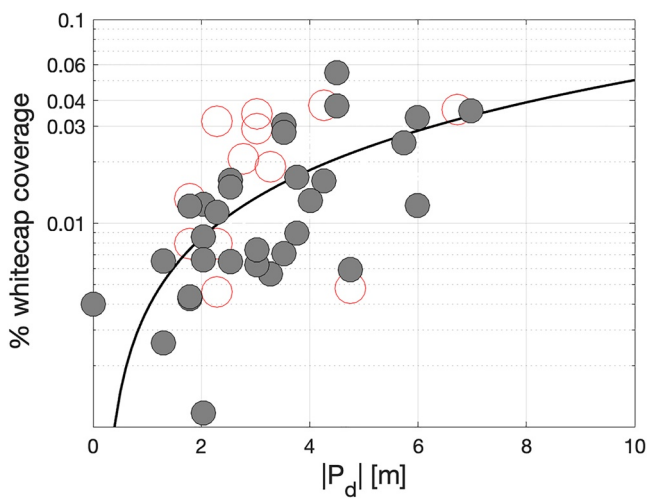

Figure 10. Whitecap fractional coverage (% whitecap coverage) versus observed penetration depths Whitecap coverage observations versus observed penetration depths. Gray circles are observations of whitecap fractional coverage determined through imaging by Brumer et al. (2017a). Red circles correspond to a spectral method by Randolph et al. (2017) attempting to capture the brightest stage of the whitecap. Solid black line shows a linear fit to the observations from digital imaging (gray circles).

breaking stages (i.e., stage A and stage B). Though observations are limited, a fit to the data suggests deeper penetration depths are linked to larger fractional whitecap coverage in the 0–6 m range. There is large uncertainty for an event-by-event approach, potentially suggesting a wave-state dependence not fully addressed here (e.g., wave slope). Figure 10, suggests there is a potential saturation in terms penetration depths relative to the surface breaking manifestation in terms of whitecaps.

5. Discussion

Measurements of ADCP backscatter anomaly were used to retrieve penetration depths of air bubbles used as tracers to define the depth of the wave affected layer. We assumed that these bubbles were directly injected by wave breaking, neglecting advective processes. The presence of these deeply penetrating bubble plumes was independently corroborated using optical methods (Randolph et al., 2013). Optical instrumentation had a bubble size resolution range of 0.5–125 μm radius, but no bubbles larger than 60 μm were detected at these depths. Void fractions were estimated to be O(10^{-8}–10^{-7}) with a significant role from small size classes (Randolph et al., 2013).

Observed penetration depths were scaled based on observations of the significant wave height and an effective wave scale (Cifuentes-Lorenzen et al., 2018). The proposed parameterization was developed based on the observed penetration depths made dimensionless by L, where L represents a relevant wave breaking scale. The dimensionless ratio was assumed proportional to the expected TKE dissipation rate enhancement relative to the wall-layer, that is, $\lvert p_d\rvert/L \propto \Gamma^{-1}$. The parameter Γ introduced the role of wave breaking through the ratio of wind-energy input relative to the predicted depth integrated law-of-the-wall TKE dissipation rate. This provided an estimate of the expected TKE dissipation rate enhancement attributable to wave breaking by assuming all energy going into the wave field (wave growth) was dissipated through wave breaking under an input-dissipation balance within the wave-affected layer. The depth the bubble transport (i.e., observed penetration depth) was linked to the depth of the TKE dissipation rate enhancement by the depth integral imbedded in the definition of Γ. The ratio Γ had a mean value of 68.4 ± 27.9 suggesting that wave breaking enhanced subsurface TKE dissipation rates by a factor of ∼70 supporting the idea of active breaking being present. Through Γ and therefore Γ^{-1} we presented a dimensionless approach to address the depth of the wave affected layer through estimates of wave-driven TKE dissipation rate enhancement and bubble plume penetration depths.

From this stand-point penetration depths were proportional to the inverse wave age (i.e., $\propto u_*/c_w$) where c_w is the effective phase speed (Equation 9) that is, $\lvert p_d\rvert/L \propto \left(\frac{u_*}{c_w}\right)\ln(L/z')$. This is consistent with previous results (e.g., Derakhti et al., 2023; Graham et al., 2004; Strand et al., 2020; Wang et al., 2016). The Γ^{-1} parameter adds weight to relevant wave field statistics and suggests a clear link between penetration depths and TKE injection mediated by wave breaking. Here, L represents a relevant wave breaking scale linked to the injection of bubbles and the depth to which the expected TKE enhancement driven by wave breaking extends. This implies that the extent of the enhancement and the injection of bubbles are both scalable by L.

It is relevant to notice that solely on dimensional grounds the following is a reasonable expectation of the observations, $\lvert p_d\rvert = f(u_*/c, L)$. Then, introducing a simple linear relationship of the form, $\lvert p_d\rvert/L \propto (u_*/c)$ leads to penetration depths directly proportional to the dimensional expression, $a\,(u_*/c)\,L$, with a a constant coefficient and L a relevant length scale for the extent of the bubble transport and or injection (e.g., Derakhti et al., 2023). From this perspective, $\lvert p_d\rvert/L \propto \left(\frac{u_*}{c_w}\right)\ln(L/z')$ is dimensionally consistent and directly proportional to the forcing expressed as the inverse wave age.

Definition of a dimensional 1:1 scaling followed by introducing two constants, $A\,\Gamma^{-1}(2\pi/k_w)$ and $B\Gamma^{-1}(H_s)$. The constant coefficients A and B were experimentally defined for the conditions presented here. Both length scales under consideration provided reasonable agreement with observations and considered representative of the wave-affected layer driven by wave-induced turbulence. Nonetheless, the effective wavelength as a length scale captures the expected shift of wind-wave coupling and wave-breaking toward higher frequencies under open ocean conditions. Furthermore, the proposed effective wavenumber better collapses the data and improves the index of agreement between observed penetration depths and the proposed parameterization. In this environment wave-driven turbulence (i.e., LC) can reach depths of $O(1/\delta)$, where δ, is the Stokes depth, $\delta = 1/2k$ and k is the wavenumber, potentially explaining the deeper observations. For example, addressing the role LC through the Langmuir number, $L_a = (u_*^w/u_s)^{0.5}$ where u_s is the Stokes drift velocity derived from the frequency spectra only for the along wind component show differences in the local wind-wave regime. The Langmuir number for period 1 and 2 have mean $\langle L_a \rangle$ values of 0.30 and 0.35 respectively placing the regime at the limit between wind and wave driven turbulence (Belcher et al., 2012). This might explain the main results in Table 6. During period 1, L_a values are as low as 0.25 suggesting a wave-turbulence driven regime potentially linking the observed small bubbles (radius ≤ 60 μm) to wave mediated transport more than to an injection followed by breaking (e.g., Czerski et al., 2022). For this period the significant wave scaling argument seems to poorly represent penetration depths and does not capture the observed variance. During the second period, $\langle L_a \rangle$ was larger shifting the regime to a wind-driven one, allowing the significant wave height to become a relevant scaling argument improving the index of agreement (Table 6). For both periods, the effective wavenumber shows to be an appropriate scaling argument.

Finally, observations of fractional whitecap coverage were plotted against the observed penetration depths. Limited observations show that deeper penetration depths appear correlated to larger whitecap coverage. While more observations are needed to address the potential decoupling of whitecap coverage and penetration depths for deeply penetrating bubbles, these results suggest that wave-driven turbulence mediated by wave breaking and the subsequent bubble injection can lead to penetration depths $O(10^0–10^1)$ m. In context of the mixed layer depth (MLD), the observed penetration depth correspond only to a fraction of the MLD of $O(10^1–10^2)$ m during the SO Gasex field campaign and exemplify the role of near surface processes.

The proposed parameterizations provide an experimental approach to address the relationship between total wave energy dissipation (i.e., TKE dissipation rate enhancement), bubble penetration depth and whitecap fractional coverage.

6. Conclusions

Two continuous segments of acoustic backscattering anomalies combined with high frequency atmospheric momentum and energy flux estimates, relevant atmospheric variables and wave statistics were used to explore the scaling of bubble penetration depths under open ocean conditions. The length scales used appear to be statistically similar, particularly in the lower penetration depth range of the observations. Nonetheless, the proposed effective wavenumber better collapses the data and improves the index of agreement between observed penetration depths and the proposed parameterization under a wider range of conditions. Results suggest that the length scale of the penetration depth is proportional to the significant wave height and the effective wavelength when weighted by the dimensionless input-dissipation ratio that is, $\Gamma^{-1} = {}^{|p_d|}/_{L}$. This ratio was used to derive dimensional scaling arguments: $A\,\Gamma^{-1}(2\pi/k_w)$ and $B\Gamma^{-1}(H_s)$ and provide a dimensional estimate for bubble penetration depths driven by wave breaking. The final parameterization can be stated as: ${}^{|p_d|}/_{L} = (A, B)\,(\alpha)^{1/2}\frac{u_*}{\kappa\, c_w}\ln\left(\frac{L}{z'}\right)$, where α is the air-water density ratio (${}^{\rho_a}/_{\rho_w}$) and L represents a relevant wave breaking scale linked to the injection of bubbles and the depth to which the expected TKE enhancement driven by wave breaking extends. This implies that the extent of the enhancement and the injection of bubbles are both scalable by L, coefficients A and B correspond to constants that satisfy a dimensional 1:1 relationship between $|p_d|$ and L. The wind-forcing dependence is clear through the inverse wave age.

Data Availability Statement

The paper relies on time series of meteorological and oceanographic data including bubble observations made with optical instrumentation and processed backscattering anomaly derived from a downward looking ADCP during the Southern Ocean Gas Exchange Experiment 2008 (SO GasEx 2008). The experiment took place in

the southern portion of the Atlantic Ocean on board of the NOAA Ship Ronald Brown (29 February–12 April 2008). The full program is stored and available at the Biological & Chemical Oceanography Data Management Office: https://www.bco-dmo.org/project/2064 and contains atmospheric and oceanographic observations made during the field campaign. The MAP-CO_2 buoy used in the paper is described in the same repository with the direct link: http://data.bco-dmo.org/jg/info/BCO/SO-GasEx/RB-08-02/MAPCO2_Buoy%7Bdir=bco-data.whoi.edu/jg/dir/BCO/SO-GasEx/RB-08-02/,data=bcodata.whoi.edu/jg/serv/BCO/SO-GasEx/RB-08-02/MAPCO2_Buoy.brev0%7D. Additionally the ADCP backscattering anomaly from the MAP-CO_2 buoy can be retrieved from: https://doi.org/10.7916/kp8r-g741. Meteorological fluxes and relevant atmospheric variables and forcing conditions are also located in the Biological & Chemical Oceanography Data Management Office: http://data.bco-dmo.org/jg/info/BCO/SO-GasEx/RB-08-02/MetFlux_Revision2%7Bdir=bcodata.whoi.edu/jg/dir/BCO/SO-GasEx/RB-08-02/,data=bcodata.whoi.edu/jg/serv/BCO/SO-GasEx/RB-08-02/MetFlux_Revision2.brev0%7D. Data processing and figures were made using the Matlab software (https://www.mathworks.com/products/matlab.html) and requires the signal processing toolbox.

Acknowledgments
This material is based upon work supported by the National Science Foundation under Grant 0647475, the National Oceanic and Atmospheric Administration under Grant NA07OAR4310084, and the NOAA Office of Climate Observations. Additional support by NSF Award (1756789) Collaborative Research: Investigating the Air-Sea Energy Exchange in the presence of Surface Gravity Waves by Measurements of Turbulence Dissipation, Production and Transport. CJ Zappa at Lamont-Doherty Earth Observatory was supported NSF through Grant Awards OCE 0647667 and OCE 1756839.
We sincerley thank the thoughtful and constructive reviews received throughout the process. The manuscript was substantially improved thanks to them.

References

Agrawal, Y. C., Terray, E. A., Donelan, M. A., Hwang, P. A., Williams, A. J., III., Drennan, W. M., et al. (1992). Enhanced dissipation of kinetic energy beneath surface waves. *Nature*, *359*(6392), 219–220. https://doi.org/10.1038/359219a0

Anguelova, M. D., & Hwang, P. A. (2016). Using energy dissipation rate to obtain active whitecap fraction. *Journal of Physical Oceanography*, *46*(2), 461–481. https://doi.org/10.1175/jpo-d-15-0069.1

Anis, A., & Moum, J. N. (1995). Surface wave-turbulence interactions. Scaling ε (z) near the sea surface. *Journal of Physical Oceanography*, *25*(9), 2025–2045. https://doi.org/10.1175/1520-0485(1995)025<2025:swisnt>2.0.co;2

Asher, W. E., & Wanninkhof, R. (1998). The effect of bubble-mediated gas transfer on purposeful dual-gaseous tracer experiments. *Journal of Geophysical Research*, *103*(C5), 10555–10560. https://doi.org/10.1029/98JC00245

Belcher, S. E., Grant, A. L., Hanley, K. E., Fox-Kemper, B., Van Roekel, L., Sullivan, P. P., et al. (2012). A global perspective on Langmuir turbulence in the ocean surface boundary layer. *Geophysical Research Letters*, *39*(18), L18605. https://doi.org/10.1029/2012GL052932

Brumer, S. E., Zappa, C. J., Blomquist, B. W., Fairall, C. W., Cifuentes-Lorenzen, A., Edson, J. B., et al. (2017b). Wave-related Reynolds number parameterizations of CO_2 and DMS transfer velocities. *Geophysical Research Letters*, *44*(19), 9865–9875. https://doi.org/10.1002/2017GL074979

Brumer, S. E., Zappa, C. J., Brooks, I. M., Tamura, H., Brown, S. M., Blomquist, B. W., et al. (2017a). Whitecap coverage dependence on wind and wave statistics as observed during SO GasEx and HiWinGS. *Journal of Physical Oceanography*, *47*(9), 2211–2235. https://doi.org/10.1175/JPO-D-17-0005.1

Burchard, H. (2001). Simulating the wave-enhanced layer under breaking surface waves with two-equation turbulence models. *Journal of Physical Oceanography*, *31*(11), 3133–3145. https://doi.org/10.1175/1520-0485(2001)031<3133:STWELU>2.0.CO;2

Cifuentes-Lorenzen, A., Edson, J. B., Zappa, C. J., & Bariteau, L. (2013). A multisensor comparison of ocean wave frequency spectra from a research vessel during the Southern Ocean gas exchange experiment. *Journal of Atmospheric and Oceanic Technology*, *30*(12), 2907–2925. https://doi.org/10.1175/JTECH-D-12-00181.1

Callaghan, A. H. (2018). On the relationship between the energy dissipation rate of surface-breaking waves and oceanic whitecap coverage. *Journal of Physical Oceanography*, *48*(11), 2609–2626. https://doi.org/10.1175/JPO-D-17-0124.1

Callaghan, A. H., Deane, G. B., & Stokes, M. D. (2016). Laboratory air-entraining breaking waves: Imaging visible foam signatures to estimate energy dissipation. *Geophysical Research Letters*, *43*(21), 11320–11328. https://doi.org/10.1002/2016GL071226

Cavaleri, L., Fox-Kemper, B., & Hemer, M. (2012). Wind waves in the coupled climate system. *Bulletin of the American Meteorological Society*, *93*(11), 1651–1661. https://doi.org/10.1175/bams-d-11-00170.1

Cifuentes-Lorenzen, A., Edson, J. B., & Zappa, C. J. (2018). Air–sea interaction in the Southern Ocean: Exploring the height of the wave boundary layer at the air–sea interface. *Boundary-Layer Meteorology*, *169*(3), 461–482. https://doi.org/10.1007/s10546-018-0376-0

Cifuentes-Lorenzen, A., & Randolph, K. (2020). The case for measuring whitecaps using ocean color and initial linkages to subsurface physics. In *Special topics in air-sea interaction*. Springer. https://doi.org/10.1007/978-3-030-36371-0_12

Craig, P. D., & Banner, M. L. (1994). Modeling wave-enhanced turbulence in the ocean surface layer. *Journal of Physical Oceanography*, *24*(12), 2546–2559. https://doi.org/10.1175/1520-0485(1994)024<2546:MWETIT>2.0.CO;2

Czerski, H., Brooks, I. M., Gunn, S., Pascal, R., Matei, A., & Blomquist, B. (2022). Ocean bubbles under high wind conditions—Part 2: Bubble size distributions and implications for models of bubble dynamics. *Ocean Science*, *18*(3), 587–608. https://doi.org/10.5194/os-18-587-2022

Dahl, P. H., & Jessup, A. T. (1995). On bubble clouds produced by breaking waves: An event analysis of ocean acoustic measurements. *Journal of Geophysical Research*, *100*(C3), 5007–5020. https://doi.org/10.1029/94JC03019

Deane, G. B., Stokes, M. D., & Callaghan, A. H. (2016). The saturation of fluid turbulence in breaking laboratory waves and implications for whitecaps. *Journal of Physical Oceanography*, *46*(3), 975–992. https://doi.org/10.1175/JPO-D-14-0187.1

Deines, K. L. (1999). Backscatter estimation using Broadband acoustic Doppler current profilers. In *Proceedings of the IEEE sixth working conference on current measurement (Cat. No.99CH36331)* (pp. 249–253). https://doi.org/10.1109/CCM.1999.755249

Derakhti, M., Thomson, J., Bassett, C. S., Malila, M. P., & Kirby, J. T. (2023). Statistics of bubble plumes generated by breaking surface waves. *ESS Open Archive*, *27*. https://doi.org/10.22541/essoar.167751591.11265648/v1

Ding, L., & Farmer, D. M. (1994). Observations of breaking surface wave statistics. *Journal of Physical Oceanography*, *24*(6), 1368–1387. https://doi.org/10.1175/1520-0485(1994)024<1368:oobsws>2.0.co;2

Drennan, W. M., Donelan, M. A., Terray, E. A., & Katsaros, K. B. (1996). Oceanic turbulence dissipation measurements in SWADE. *Journal of Physical Oceanography*, *26*(5), 808–815. https://doi.org/10.1175/1520-0485(1996)026<0808:OTDMIS>2.0.CO;2

Drennan, W. M., Kahma, K. K., Terray, E. A., Donelan, M. A., & Kitaigorodskii, S. A. (1992). Observations of the enhancement of kinetic energy dissipation beneath breaking wind waves. In M. L. Banner, & R. H. J. Grimshaw (Eds.), *Breaking waves. International union of theoretical and applied mechanics*. Springer. https://doi.org/10.1007/978-3-642-84847-6_6

Edson, J. B., Fairall, C. W., Bariteau, L., Zappa, C. J., Cifuentes-Lorenzen, A., McGillis, W. R., et al. (2011). Direct covariance measurement of CO_2 gas transfer velocity during the 2008 Southern Ocean gas exchange experiment: Wind speed dependency. *Journal of Geophysical Research*, *116*, C00F10. https://doi.org/10.1029/2011JC007022

Edson, J. B., Hinton, A. A., Prada, K. E., Hare, J. E., & Fairall, C. W. (1998). Direct covariance flux estimates from mobile platforms at sea. *Journal of Atmospheric and Oceanic Technology*, *15*(2), 547–562. https://doi.org/10.1175/1520-0426(1998)015<0547:dcfefm>2.0.co;2

Farmer, D. M., McNeil, C. L., & Johnson, B. D. (1993). Evidence for the importance of bubbles in increasing air–sea gas flux. *Nature*, *361*(6413), 620–623. https://doi.org/10.1038/361620a0

Gargett, A. E., & Wells, J. R. (2007). Langmuir turbulence in shallow water. Part 1. Observations. *Journal of Fluid Mechanics*, *576*, 27–61. https://doi.org/10.1017/S0022112006004575

Gemmrich, J. (2005). On the occurrence of wave breaking. In *Rogue waves: Proceedings 14th'Aha Huliko'a Hawaiian winter workshop* (pp. 123–130). University of Hawaii at Manoa.

Gemmrich, J. R., Banner, M. L., & Garrett, C. (2008). Spectrally resolved energy dissipation rate and momentum flux of breaking waves. *Journal of Physical Oceanography*, *38*(6), 1296–1312. https://doi.org/10.1175/2007JPO3762.1

Gemmrich, J. R., & Farmer, D. M. (1999). Observations of the scale and occurrence of breaking surface waves. *Journal of Physical Oceanography*, *29*(10), 2595–2606. https://doi.org/10.1175/1520-0485(1999)029<2595:ootsao>2.0.co;2

Gemmrich, J. R., & Farmer, D. M. (2004). Near-surface turbulence in the presence of breaking waves. *Journal of Physical Oceanography*, *34*(5), 1067–1086. https://doi.org/10.1175/1520-0485(2004)034<1067:NTITPO>2.0.CO;2

Gemmrich, J. R., Mudge, T. D., & Polonichko, V. D. (1994). On the energy input from wind to surface waves. *Journal of Physical Oceanography*, *24*(11), 2413–2417. https://doi.org/10.1175/1520-0485(1994)024<2413:OTEIFW>2.0.CO;2

Graham, A., Woolf, D. K., & Hall, A. J. (2004). Aeration due to breaking waves. Part I: Bubble populations. *Journal of Physical Oceanography*, *34*(5), 989–1007. https://doi.org/10.1175/1520-0485(2004)034<0989:ADTBWP>2.0.CO;2

Ho, D. T., Sabine, C. L., Hebert, D., Ullman, D. S., Wanninkhof, R., Hamme, R. C., et al. (2011). Southern Ocean gas exchange experiment: Setting the stage. *Journal of Geophysical Research*, *116*, C00F08. https://doi.org/10.1029/2010JC006852

Kitaigorodskii, S. A. (1998). The dissipation subrange in wind-wave spectra. *Geophysica Finland*, *34*(3), 179–207.

Kukulka, T., & Brunner, K. (2015). Passive buoyant tracers in the ocean surface boundary layer: 1. Influence of equilibrium wind-waves on vertical distributions. *Journal of Geophysical Research: Oceans*, *120*(5), 3837–3858. https://doi.org/10.1002/2014JC010487

Lamarre, E., & Melville, W. (1991). Air entrainment and dissipation in breaking waves. *Nature*, *351*(6326), 469–472. https://doi.org/10.1038/351469a0

Leibovich, S. (1983). The form and dynamics of Langmuir circulations. *Annual Review of Fluid Mechanics*, *15*(1), 391–427. https://doi.org/10.1146/annurev.fl.15.010183.002135

Li, Q., & Fox-Kemper, B. (2017). Assessing the effects of Langmuir turbulence on the entrainment buoyancy flux in the ocean surface boundary layer. *Journal of Physical Oceanography*, *47*(12), 2863–2886. https://doi.org/10.1175/JPO-D-17-0085.1

Li, S., Li, M., Gerbi, G. P., & Song, J.-B. (2013). Roles of breaking waves and Langmuir circulation in the surface boundary layer of a coastal ocean. *Journal of Geophysical Research: Oceans*, *118*(10), 5173–5187. https://doi.org/10.1002/jgrc.20387

McWilliams, J., Sullivan, P., & Moeng, C. H. (1997). Langmuir turbulence in the ocean. *Journal of Fluid Mechanics*, *334*, 1–30. https://doi.org/10.1017/s0022112096004375

Melville, W. K. (1996). The role of surface-wave breaking in air-sea interaction. *Annual Review of Fluid Mechanics*, *28*(1), 279–321. https://doi.org/10.1146/annurev.fl.28.010196.001431

Moore, T. S., DeGrandpre, M. D., Sabine, C. L., Hamme, R. C., Zappa, C. J., McGillis, W. R., et al. (2011). Sea surface PCO_2 and O_2 in the Southern Ocean during the Austral Fall, 2008. *Journal of Geophysical Research*, *116*(C4), C00F11. https://doi.org/10.1029/2010JC006560

Plueddemann, A. J., Smith, J. A., Farmer, D. M., Weller, R. A., Crawford, W. R., Pinkel, R., et al. (1996). Structure and variability of Langmuir circulation during the surface waves processes program. *Journal of Geophysical Research*, *101*(C2), 3525–3543. https://doi.org/10.1029/95JC03282

Randolph, K., Dierssen, H. M., Cifuentes-Lorenzen, A., Balch, W. M., Monahan, E. C., Zappa, C. J., et al. (2017). Novel methods for optically measuring whitecaps under natural wave-breaking conditions in the Southern Ocean. *Journal of Atmospheric and Oceanic Technology*, *34*(3), 533–554. https://doi.org/10.1175/jtech-d-16-0086.1

Randolph, K., M Dierssen, H., Twardowski, M., Cifuentes-Lorenzen, A., & Zappa, C. J. (2013). Optical measurements of small deeply penetrating bubble populations generated by breaking waves in the Southern Ocean. *Journal of Geophysical Research: Oceans*, *119*(2), 757–776. https://doi.org/10.1002/2013jc009227

Rapp, R. J., & Melville, W. K. (1990). Laboratory measurements of deep-water breaking waves. *Philosophical Transactions of the Royal Society of London—Series A: Mathematical and Physical Sciences*, *331*, 735–800.

Schwendeman, M., & Thomson, J. (2015). Observations of whitecap coverage and the relation to wind stress, wave slope, and turbulent dissipation. *Journal of Geophysical Research: Oceans*, *120*(12), 8346–8363. https://doi.org/10.1002/2015jc011196

Schwendeman, M., Thomson, J., & Gemmrich, J. R. (2014). Wave breaking dissipation in a young wind sea. *Journal of Physical Oceanography*, *44*(1), 104–127. https://doi.org/10.1175/jpo-d-12-0237.1

Strand, K. O., Breivik, Ø., Pedersen, G., Vikebø, F. B., Sundby, S., & Christensen, K. H. (2020). Long-term statistics of observed bubble depth versus modeled wave dissipation. *Journal of Geophysical Research: Oceans*, *125*(2), e2019JC015906. https://doi.org/10.1029/2019JC015906

Sullivan, P., McWilliams, J., & Kendall Melville, W. (2007). Surface gravity wave effects in the oceanic boundary layer: Large-eddy simulation with vortex force and stochastic breakers. *Journal of Fluid Mechanics*, *593*, 405–452. https://doi.org/10.1017/S002211200700897X

Sutherland, P., & Kendall Melville, W. (2015). Field measurements of surface and near-surface turbulence in the presence of breaking waves. *Journal of Physical Oceanography*, *45*(4), 943–965. https://doi.org/10.1175/JPO-D-14-0133.1

Terray, E. A., Ma, D., Agrawal, Y. C., Drennan, W. M., Kahma, K. K., Williams, A. J., et al. (1996). Estimates of kinetic energy dissipation under breaking waves. *Journal of Physical Oceanography*, *26*(5), 792–807. https://doi.org/10.1175/1520-0485(1996)026<0792:EOKEDU>2.0.CO;2

Thomson, J., Schwendeman, M. S., Zippel, S. F., Moghimi, S., Gemmrich, J., & Rogers, W. E. (2016). Wave-breaking turbulence in the ocean surface layer. *Journal of Physical Oceanography*, *46*(6), 1857–1870. https://doi.org/10.1175/JPO-D-15-0130.1

Thorpe, S. (1986). Measurements with an automatically recording inverted echo sounder; ARIES and the bubble clouds. *Journal of Physical Oceanography*, *16*(8), 1462–1478. https://doi.org/10.1175/1520-0485(1986)016,1462:MWAARI.2.0.CO;2

Thorpe, S. A. (1992). Bubble clouds and the dynamics of the upper ocean. *Quarterly Journal of the Royal Meteorological Society*, *118*(503), 1–22. https://doi.org/10.1002/qj.49711850302

Trevorrow, M. V. (2003). Measurements of near-surface bubble plumes in the open ocean with implications for high-frequency sonar performance. *Journal of the Acoustical Society of America*, *114*(5), 2672–2684. https://doi.org/10.1121/1.1621008

Vagle, S., McNeil, C., & Steiner, N. (2010). Upper ocean bubble measurements from the NE Pacific and estimates of their role in air-sea gas transfer of the weakly soluble gases nitrogen and oxygen. *Journal of Geophysical Research*, *115*(C12), C12054. https://doi.org/10.1029/2009JC005990

Wang, D. W., Wijesekera, H. W., Jarosz, E., Teague, W. J., & Pegau, W. S. (2016). Turbulent diffusivity under high winds from acoustic measurements of bubbles. *Journal of Physical Oceanography*, *46*(5), 1593–1613. https://doi.org/10.1175/jpo-d-15-0164.1

Willmott, C. J., Ackleson, S. G., Davis, R. E., Feddema, J. J., Klink, K. M., Legates, D. R., et al. (1985). Statistics for the evaluation and comparison of models. *Journal of Geophysical Research*, *90*(C5), 8995–9005. https://doi.org/10.1029/JC090iC05p08995

Woolf, D. K. (2005). Parametrization of gas transfer velocities and sea-state-dependent wave breaking. *Tellus B: Chemical and Physical Meteorology*, *57*(2), 87–94. https://doi.org/10.1111/j.1600-0889.2005.00139.x

Wu, L., Breivik, Ø., & Anna, R. (2019). Ocean-wave-atmosphere interaction processes in a fully coupled modeling system. *Journal of Advances in Modeling Earth Systems*, *11*(11), 3852–3874. https://doi.org/10.1029/2019MS001761

Zappa, C. J., Banner, M. L., Morison, R. P., & Brumer, S. E. (2016). On the variation of the effective breaking strength in oceanic sea states. *Journal of Physical Oceanography*, *46*(7), 2049–2061. https://doi.org/10.1175/jpo-d-15-0227.1

Zappa, C. J., McGillis, W. R., Raymond, P. A., Edson, J. B., Hintsa, E. J., Zemmelink, H. J., et al. (2007). Environmental turbulent mixing controls on air-water gas exchange in marine and aquatic systems. *Geophysical Research Letters*, *34*(10), L10601. https://doi.org/10.1029/2006GL028790

Zavarsky, A., Goddijn-Murphy, L., Steinhoff, T., & Marandino, C. A. (2018). Bubble-mediated gas transfer and gas transfer suppression of DMS and CO_2. *Journal of Geophysical Research: Atmospheres*, *123*(12), 6624–6647. https://doi.org/10.1029/2017JD028071